Journal of Science and Technology in Civil Engineering, HUCE, 2026, 20 (3): 108–126

EXPERIMENTAL AND SEMI-ANALYTICAL INVESTIGATION OF DYNAMIC BEHAVIOR OF SANDWICH PLATES WITH POROUS CORE AND CFRP FACE SHEETS

Hoang-Nam Nguyen[a], Thanh-Tung Pham[a,*], Minh-Tu Tran[a]

[a]*Faculty of Civil and Industrial construction, Hanoi University of Civil Engineering, 55 Giai Phong road, Bach Mai ward, Hanoi, Vietnam*

Article history:
Received 14/5/2026, Revised 08/6/2026, Accepted 16/7/2026, Available online 25/9/2026, Version of Record 25/9/2026

Abstract

This paper presents an experimental and theoretical investigation of the vibration behavior of sandwich plates consisting of an Expanded Polystyrene (EPS) porous concrete core and carbon fiber-reinforced polymer (CFRP) face sheets. For the theoretical study, Reddy's third-order shear deformation theory (RTSDT), combined with the pb-2 Ritz method, is employed to formulate the governing equations, from which natural frequencies are obtained via eigenvalue analysis and dynamic responses are computed using the Newmark integration scheme. The numerical model is validated against established benchmarks. For the experimental study, rectangular sandwich plate specimens with CFRP layups are fabricated and tested under two opposite edges simply supported and the remaining two edges free (SFSF) boundary conditions. The fundamental natural frequencies are measured using step-release free vibration tests with five accelerometers and Fast Fourier Transform (FFT) analysis. The experimentally obtained natural frequencies are then compared with the semi-analytical predictions. The comparison shows a consistent trend between the experimental measurements and semi-analytical predictions. The outcomes of this study can be valuable for the design and analysis of lightweight sandwich plates with porous cores and composite face sheets.

Keywords: porous sandwich plates; EPS concrete; CFRP face sheets; experimental dynamic testing; Ritz method; third-order shear deformation theory.

1. Introduction

Sandwich structures, consisting of a porous core layer bonded between two thin face sheets, constitute an efficient structural configuration for lightweight engineering applications. In such structures, the high-stiffness face sheets primarily resist bending and in-plane loads, whereas the relatively thick, porous core sustains transverse shear stresses, stabilizes the faces against buckling, and significantly reduces the overall structural weight. Moreover, the presence of porosity enhances multifunctional performance by improving thermal insulation, acoustic attenuation, and vibration damping characteristics. Owing to these combined mechanical and functional advantages, sandwich structures have been widely adopted in diverse fields, including building construction, transportation, aerospace, and defense applications [1–3].

Extensive theoretical investigations of sandwich structures with porous cores have been conducted in recent years, with particular emphasis on their dynamic and stability characteristics. Rezaei and Saidi [4] utilized Reddy's third-order shear deformation theory (RTSDT) to quantify the effects of porosity on natural frequencies of thick rectangular porous plates. Wattanasakulpong and

*Corresponding author. *E-mail address:* tungpt@huce.edu.vn (Pham, T.-T.)
https://doi.org/10.31814/stce.huce2026-20(3)-06 p-ISSN 1859-2996; e-ISSN 2734-9268
© 2026 The Author(s). Published by Hanoi University of Civil Engineering. Licensed under CC BY-NC-ND 4.0.

Eiadtrong [5] examined transient responses of sandwich plates with a functionally graded porous (FGP) core using the Jacobi–Ritz method, demonstrating the effectiveness of semi-analytical approaches in capturing time-dependent behavior. Yüksel and Akbaş [6] studied vibration behavior of sandwich plates with laminated face sheets and porous cores on Winkler-Pasternak elastic foundations, thereby incorporating foundation-structure interaction effects. Thang et al. [7] presented elastic buckling and free vibration analyses of porous-cellular plates with different porosity distributions, revealing the role of porosity gradation in structural stability. Based on TSDT, Dat et al. [8] investigated vibration and nonlinear dynamic analysis of sandwich plates with FG-CNTRC skins and a porous core using Galerkin method and Runge–Kutta method. Li et al. [9] combined FSDT with experimental vibro-acoustic measurements to evaluate the free vibration and damping characteristics of porous foam FRP sandwich plates, bridging theoretical modeling and experimental validation. Li et al. [10] investigated the vibration response and stability of functionally graded porous (FGP) sandwich plates subjected to a moving mass using a four-variable equivalent-single-layer (ESL) plate theory, highlighting the effects of various porosity distribution patterns and moving mass characteristics. Safaei [11] studied frequency-dependent damped vibrations of multifunctional foam sandwich plates, emphasizing the importance of material multifunctionality. Collectively, these studies establish that porosity distribution and porosity coefficient are critical parameters governing the dynamic behavior of sandwich plates.

Carbon fiber-reinforced polymer (CFRP) plays an increasingly important role in structural design due to its superior specific strength, low weight, and long-term durability. Numerous studies have demonstrated the effectiveness of CFRP in improving structural stiffness and strength [12, 13]. The combination of a porous core with CFRP face sheets creates a synergistic composite structure where the lightweight, energy-absorbing core provides acoustic and thermal benefits, while the high-stiffness CFRP skins provide load-bearing capacity and structural rigidity.

Although extensive theoretical analyses of porous sandwich structures have been reported, experimental investigations remain relatively limited. Jasion et al. [14] combined theoretical and experimental studies on buckling and wrinkling behavior of sandwich beams and circular plates with a metal foam core, providing early validation of stability predictions. Sokolinsky et al. [15, 16] conducted four-point bending tests alongside analytical modeling of sandwich beams with aluminum face sheets and Divinycell foam cores, subsequently extending the work to free vibration analysis, thereby offering a comprehensive assessment of both static and dynamic responses. Dariushi and Sadighi [17] investigated geometrically nonlinear bending of sandwich beams with glass/epoxy faces and a polymeric core through an integrated analytical and experimental approach. With regard to plate-type structures, Njim et al. [18] presented a combined analytical and experimental free vibration study of 3D-printed FGP sandwich plates with homogeneous skins, reporting discrepancies of up to 15 % between theoretical predictions and experimental results. Yurddaskal et al. [19] experimentally determined how curvature and foam properties affect natural frequencies of sandwich panels with E-glass/epoxy faces and PVC foam cores. Zhang et al. [20] further extended the analysis to thermo-mechanical coupling by examining the thermal vibration characteristics of FRP sandwich plates with ceramic foam cores. In the context of national study, Hung et al. [21] conducted experimental measurements of natural frequencies, bending responses, and time-history behavior for a cantilever porous sandwich beam with an expanded polystyrene (EPS) concrete core and cemboard face sheets, and validated the results against mesh-free numerical predictions.

The literature review indicates that, although the theoretical modelling of porous sandwich structures has been extensively developed, corresponding experimental validation remains limited, partic-

ularly for plate configurations with composite face sheets. Consequently, further research is required to bridge the gap between predictive theoretical models and experimentally observed structural behavior.

This paper investigates the free vibration and dynamic response of sandwich plates with a uniform porous core and CFRP face sheets through combined theoretical and experimental approaches. For theoretical study, the pb-2 Ritz method based on the principle of minimum potential energy is employed to derive the governing equations; the natural frequencies are subsequently obtained via eigenvalue analysis, while the acceleration-time responses are computed using the Newmark integration scheme. Experimentally, the fundamental natural frequencies and acceleration-time histories of sandwich plate specimens under SFSF boundary conditions are subsequently compared with the corresponding semi-analytical predictions.

2. Theoretical formulation

Consider a rectangular sandwich plate with dimensions $a \times b$ in the xy-plane and total thickness h in the z-direction. The plate comprises an FGP core of thickness h_c sandwiched between two CFRP face sheets, each of thickness h_f ($h = h_c + 2h_f$). A Cartesian coordinate system (x, y, z) is defined with the x- and y-axes located in the mid-plane, while the z-axis is oriented upward from the plate surface. The formulation is based on the following assumptions: (i) both the face sheets and the core behave as linearly elastic materials, and (ii) perfect bonding exists between the layers, ensuring no interfacial slip.

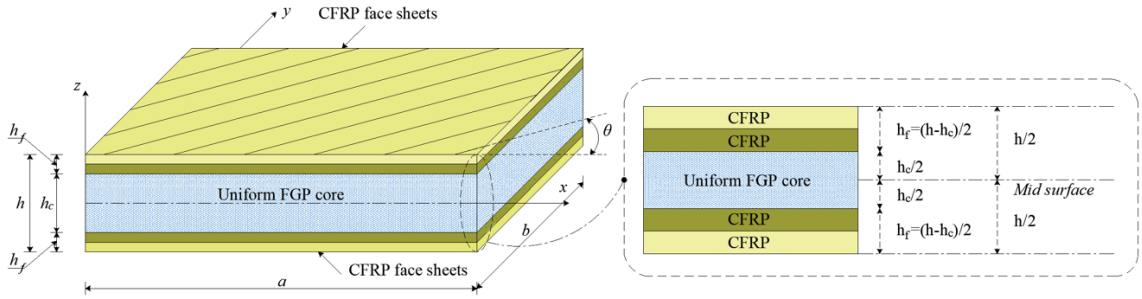


Figure 1. Sandwich plate geometry and coordinate system

2.1. *Effective material property modelling*

The porous core is characterized by a uniform distribution of porosity across its thickness. Accordingly, the effective mechanical properties, namely Young's modulus E, shear modulus G, and mass density ρ are assumed to be constant along the thickness direction and are given as follows [1]:

$$E = E_1(1 - e_0); \quad G = \frac{E(z)}{2(1+\nu)}; \quad \rho = \rho_1(1 - e_m); \quad -\frac{h_c}{2} \le z \le \frac{h_c}{2} \tag{1}$$

where (E_1, ρ_1) are the Young's modulus and mass density of the non-porous matrix material and (E_2, ρ_2) are the effective modulus and density of the porous material, respectively. Poisson's ratio ν is assumed to be constant. The porosity coefficient e_0 and mass density coefficient e_m are defined as [1]:

$$e_0 = 1 - \frac{E_2}{E_1}; \quad e_m = 1 - \frac{\rho_2}{\rho_1} \tag{2}$$

The relationship between the porosity coefficient and the mass density coefficient depends on the morphology of the cellular microstructure. According to Gibson [22], porous materials are classified

into two categories based on whether the individual cells are interconnected (open-cell) or isolated (closed-cell). For each type, the relationship between elastic modulus and density is expressed as follows [1]:

$$\begin{aligned} \frac{E_2}{E_1} &= \left(\frac{\rho_2}{\rho_1}\right)^2 \quad \text{(open-cell)} \\ \frac{E_2}{E_1} &= \left(\frac{\rho_2/\rho_1 + 0.121}{1.121}\right)^{2.3} \quad \text{(closed-cell)} \end{aligned} \tag{3}$$

Combining Eqs. (2) and (3), yields the relationship between e_0 and e_m as follows:

$$\begin{aligned} e_m &= 1 - \sqrt{1 - e_0} \quad \text{(open-cell)} \\ e_m &= 1.121\left(1 - \sqrt[2.3]{1 - e_0}\right) \quad \text{(closed-cell)} \end{aligned} \tag{4}$$

In open-cell foams, the pores are interconnected, whereas in closed-cell foams each pore is fully enclosed by continuous cell walls. The EPS concrete core used in this study exhibits a closed-cellular microstructure [23]. Accordingly, the open-cell model is adopted in the benchmark studies in Section 3 to ensure consistency with the reference data, while the closed-cell model is used in the experimental validation discussed in Section 4.

The CFRP face sheets are modeled as orthotropic laminates. The mechanical properties of each lamina in the principal material directions are denoted by E_{11}, E_{22}, G_{12}, G_{13}, G_{23}, ν_{12}, ν_{21}. For an off-axis ply oriented at angle φ to the global x-axis, the reduced stiffness coefficients Q_{ij} defined in the material coordinate system are transformed into the global coordinate system as $\bar{Q}_{ij}$ using the standard coordinate transformation [24].

2.2. *Displacement field and strain–displacement relations*

The displacement field according to Reddy's third-order shear deformation theory (RTSDT) is assumed as follows [24]:

$$\begin{aligned} u(x,y,z,t) &= u_0(x,y,t) + z\theta_x(x,y,t) + c_1 z^3\left(\theta_x + \frac{\partial w_0}{\partial x}\right) \\ v(x,y,z,t) &= v_0(x,y,t) + z\theta_y(x,y,t) + c_1 z^3\left(\theta_y + \frac{\partial w_0}{\partial y}\right) \\ w(x,y,z,t) &= w_0(x,y,t) \end{aligned} \tag{5}$$

where u_0, v_0, w_0 denote the mid-plane displacements in the x-, y-, and z-directions, respectively; θ_x and θ_y represent the rotations of the transverse normal about the y- and x-axes, respectively; and $c_1 = 4/(3h^2)$.

The strain components are derived from the displacement–strain relations of elasticity as follows:

$$\begin{aligned} \begin{Bmatrix} \varepsilon_x \\ \varepsilon_y \\ \gamma_{xy} \end{Bmatrix} &= \begin{Bmatrix} \varepsilon_x^{(0)} \\ \varepsilon_y^{(0)} \\ \gamma_{xy}^{(0)} \end{Bmatrix} + z\begin{Bmatrix} \varepsilon_x^{(1)} \\ \varepsilon_y^{(1)} \\ \gamma_{xy}^{(1)} \end{Bmatrix} + z^3\begin{Bmatrix} \varepsilon_x^{(3)} \\ \varepsilon_y^{(3)} \\ \gamma_{xy}^{(3)} \end{Bmatrix} \\ \begin{Bmatrix} \gamma_{yz} \\ \gamma_{xz} \end{Bmatrix} &= \begin{Bmatrix} \gamma_{yz}^{(0)} \\ \gamma_{xz}^{(0)} \end{Bmatrix} + z^2\begin{Bmatrix} \gamma_{yz}^{(2)} \\ \gamma_{xz}^{(2)} \end{Bmatrix} \end{aligned} \tag{6}$$

where

$$\begin{Bmatrix} \varepsilon_x^{(0)} \\ \varepsilon_y^{(0)} \\ \gamma_{xy}^{(0)} \end{Bmatrix} = \begin{Bmatrix} \dfrac{\partial u_0}{\partial x} \\ \dfrac{\partial v_0}{\partial y} \\ \dfrac{\partial u_0}{\partial y} + \dfrac{\partial v_0}{\partial x} \end{Bmatrix}; \quad \begin{Bmatrix} \varepsilon_x^{(1)} \\ \varepsilon_y^{(1)} \\ \gamma_{xy}^{(1)} \end{Bmatrix} = \begin{Bmatrix} \dfrac{\partial \theta_x}{\partial x} \\ \dfrac{\partial \theta_y}{\partial y} \\ \dfrac{\partial \theta_x}{\partial y} + \dfrac{\partial \theta_y}{\partial x} \end{Bmatrix}; \quad \begin{Bmatrix} \varepsilon_x^{(3)} \\ \varepsilon_y^{(3)} \\ \gamma_{xy}^{(3)} \end{Bmatrix} = -c_1 \begin{Bmatrix} \dfrac{\partial \theta_x}{\partial x} + \dfrac{\partial^2 w_0}{\partial x^2} \\ \dfrac{\partial \theta_y}{\partial y} + \dfrac{\partial^2 w_0}{\partial y^2} \\ \dfrac{\partial \theta_x}{\partial y} + \dfrac{\partial \theta_y}{\partial x} + 2\dfrac{\partial^2 w_0}{\partial x \partial y} \end{Bmatrix}$$

$$\begin{Bmatrix} \gamma_{xz}^{(0)} \\ \gamma_{yz}^{(0)} \end{Bmatrix} = \begin{Bmatrix} \theta_x + \dfrac{\partial w_0}{\partial x} \\ \theta_y + \dfrac{\partial w_0}{\partial y} \end{Bmatrix}; \quad \begin{Bmatrix} \gamma_{xz}^{(2)} \\ \gamma_{yz}^{(2)} \end{Bmatrix} = -3c_1 \begin{Bmatrix} \theta_x + \dfrac{\partial w_0}{\partial x} \\ \theta_y + \dfrac{\partial w_0}{\partial y} \end{Bmatrix}$$

It should be noted that, the in-plane strains ε_x, ε_y, γ_{xy} consist of membrane, bending, and higher-order contributions, whereas the transverse shear strains γ_{xz}, γ_{yz} are expressed in terms of the rotations and their higher-order corrections.

2.3. Constitutive relations and stress resultants

The stress-strain relationship in the k-th layer follows Hooke's law. Since the sandwich plate comprises layers with distinct material types, the reduced stiffness coefficients must be determined separately for the porous core and the CFRP face sheets.

For the FGP core layer ($k = C$), the reduced stiffness coefficients are determined from the porosity-dependent elastic modulus $E(z)$ and Poisson's ratio ν as:

$$Q_{11}^{(C)} = Q_{22}^{(C)} = \frac{E(z)}{1-\nu^2}; \quad Q_{12}^{(C)} = \nu Q_{11}^{(C)}; \quad Q_{66}^{(C)} = Q_{44}^{(C)} = Q_{55}^{(C)} = G(z)$$

For each CFRP ply, the material is assumed to be orthotropic in its principal coordinate system. The reduced stiffness coefficients in the material axes are given by [24]:

$$Q_{11} = \frac{E_{11}}{1-\nu_{12}\nu_{21}}; \quad Q_{22} = \frac{E_{22}}{1-\nu_{12}\nu_{21}}; \quad Q_{12} = \nu_{12}Q_{22};$$
$$Q_{66} = G_{12}; \quad Q_{44} = G_{23}; \quad Q_{55} = G_{13}$$

When a local principal coordinate axes of an individual lamina are oriented at an angle φ relative to the global plate coordinate system, the reduced stiffness coefficients defined in the material coordinate system are transformed into the global coordinates using the following transformation relations [24]:

$$\begin{aligned}
\bar{Q}_{11} &= Q_{11}\cos^4\varphi + 2(Q_{12}+2Q_{66})\sin^2\varphi\cos^2\varphi + Q_{22}\sin^4\varphi \\
\bar{Q}_{12} &= (Q_{11}+Q_{22}-4Q_{66})\sin^2\varphi\cos^2\varphi + Q_{12}(\sin^4\varphi+\cos^4\varphi) \\
\bar{Q}_{22} &= Q_{11}\sin^4\varphi + 2(Q_{12}+2Q_{66})\sin^2\varphi\cos^2\varphi + Q_{22}\cos^4\varphi \\
\bar{Q}_{16} &= (Q_{11}-Q_{12}-2Q_{66})\sin\varphi\cos^3\varphi + (Q_{12}-Q_{22}+2Q_{66})\sin^3\varphi\cos\varphi \\
\bar{Q}_{26} &= (Q_{11}-Q_{12}-2Q_{66})\sin^3\varphi\cos\varphi + (Q_{12}-Q_{22}+2Q_{66})\sin\varphi\cos^3\varphi \\
\bar{Q}_{66} &= (Q_{11}+Q_{22}-2Q_{12}-2Q_{66})\sin^2\varphi\cos^2\varphi + Q_{66}(\sin^4\varphi+\cos^4\varphi) \\
\bar{Q}_{44} &= Q_{44}\cos^2\varphi + Q_{55}\sin^2\varphi; \quad \bar{Q}_{55} = Q_{55}\cos^2\varphi + Q_{44}\sin^2\varphi; \\
\bar{Q}_{45} &= (Q_{55}-Q_{44})\sin\varphi\cos\varphi
\end{aligned}$$

Once the transformed stiffness coefficients are established for all layers, the stress components within the k-th layer can be expressed in a matrix form as follows:

$$\begin{Bmatrix} \sigma_x \\ \sigma_y \\ \tau_{xy} \\ \tau_{yz} \\ \tau_{xz} \end{Bmatrix}^{(k)} = \begin{bmatrix} \bar{Q}_{11} & \bar{Q}_{12} & \bar{Q}_{16} & 0 & 0 \\ \bar{Q}_{12} & \bar{Q}_{22} & \bar{Q}_{26} & 0 & 0 \\ \bar{Q}_{16} & \bar{Q}_{26} & \bar{Q}_{66} & 0 & 0 \\ 0 & 0 & 0 & \bar{Q}_{44} & \bar{Q}_{45} \\ 0 & 0 & 0 & \bar{Q}_{45} & \bar{Q}_{55} \end{bmatrix}^{(k)} \begin{Bmatrix} \varepsilon_x \\ \varepsilon_y \\ \gamma_{xy} \\ \gamma_{yz} \\ \gamma_{xz} \end{Bmatrix} \tag{7}$$

The in-plane force resultants, bending moments, and higher-order stress resultants are obtained by integrating the stresses through the plate thickness according to RTSDT formulation:

$$\begin{Bmatrix} N_x, & M_x, & P_x \\ N_y, & M_y, & P_y \\ N_{xy}, & M_{xy}, & P_{xy} \end{Bmatrix} = \sum_{k=1}^{N_L} \int_{z_k}^{z_{k+1}} \begin{Bmatrix} \sigma_x \\ \sigma_y \\ \sigma_{xy} \end{Bmatrix} \left\{1, z, z^3\right\} dz$$
$$\begin{Bmatrix} Q_x & R_x \\ Q_y & R_y \end{Bmatrix} = \sum_{i=1}^{N_L} \int_{z_k}^{z_{k+1}} \begin{Bmatrix} \sigma_{xz} \\ \sigma_{yz} \end{Bmatrix} \left\{1, z^2\right\} dz \tag{8}$$

where N_L is the total number of layers (core and individual CFRP plies), and z_k, z_{k+1} denote the bottom and top z-coordinates of the k-th layer.

These resultants are related to the mid-plane strains and curvatures through the plate stiffness coefficients, which are defined as:

$$\begin{Bmatrix} \{N\} \\ \{M\} \\ \{P\} \end{Bmatrix} = \begin{bmatrix} [A] & [B] & [E] \\ [B] & [D] & [F] \\ [E] & [F] & [H] \end{bmatrix} \begin{Bmatrix} \{\varepsilon^{(0)}\} \\ \{\varepsilon^{(1)}\} \\ \{\varepsilon^{(3)}\} \end{Bmatrix}; \quad \begin{Bmatrix} \{Q\} \\ \{R\} \end{Bmatrix} = \begin{bmatrix} [\bar{A}] & [\bar{D}] \\ [\bar{D}] & [\bar{F}] \end{bmatrix} \begin{Bmatrix} \{\gamma^{(0)}\} \\ \{\gamma^{(2)}\} \end{Bmatrix} \tag{9}$$

where A_{ij}, B_{ij}, D_{ij}, E_{ij}, F_{ij} and H_{ij} are determined as follows:

$$(A_{ij},\, B_{ij},\, D_{ij},\, E_{ij},\, F_{ij},\, H_{ij}) = \sum_{k=1}^{N_L} \int_{z_k}^{z_{k+1}} \bar{Q}_{ij}^{(k)} \left(1,\, z,\, z^2,\, z^3,\, z^4,\, z^6\right) dz$$
$$(A_{ij}^s,\, B_{ij}^s,\, D_{ij}^s) = \sum_{k=1}^{N_L} \int_{z_k}^{z_{k+1}} \bar{Q}_{ij}^{(k)} \left(1,\, z^2,\, z^4\right) dz; \quad i, j = 4, 5$$

2.4. Energy expressions

The total energy functional of FGP-FRP sandwich plate can be formulated as:

$$\Pi = T - U - W \tag{10}$$

in which, the strain energy U is given by:

$$U = \frac{1}{2} \int_0^a \int_0^b \begin{Bmatrix} \varepsilon^{(0)T} A\, \varepsilon^{(0)} + 2\, \varepsilon^{(0)T} B\, \varepsilon^{(1)} + 2\, \varepsilon^{(0)T} E\, \varepsilon^{(3)} \\ + \varepsilon^{(1)T} D\, \varepsilon^{(1)} + 2\, \varepsilon^{(1)T} F\, \varepsilon^{(3)} + \varepsilon^{(3)T} H\, \varepsilon^{(3)} \\ + \gamma^{(0)T} A^s \gamma^{(0)} + 2\, \gamma^{(0)T} B^s \gamma^{(2)} + \gamma^{(2)T} D^s \gamma^{(2)} \end{Bmatrix} dx\, dy \tag{11}$$

The kinetic energy T takes the form:

$$T = \frac{1}{2}\int_0^a \int_0^b \left\{ \begin{array}{l} I_0(\dot{u}_0^2 + \dot{v}_0^2 + \dot{w}_0^2) + 2I_1(\dot{u}_0\dot{\theta}_x + \dot{v}_0\dot{\theta}_y) + I_2(\dot{\theta}_x^2 + \dot{\theta}_y^2) \\ -2c_1 I_3\left[\dot{u}_0\left(\dot{\theta}_x + \dfrac{\partial \dot{w}_0}{\partial x}\right) + \dot{v}_0\left(\dot{\theta}_y + \dfrac{\partial \dot{w}_0}{\partial y}\right)\right] \\ -2c_1 I_4\left[\dot{\theta}_x\left(\dot{\theta}_x + \dfrac{\partial \dot{w}_0}{\partial x}\right) + \dot{\theta}_y\left(\dot{\theta}_y + \dfrac{\partial \dot{w}_0}{\partial y}\right)\right] \\ + c_1^2 I_6\left[\left(\dot{\theta}_x + \dfrac{\partial \dot{w}_0}{\partial x}\right)^2 + \left(\dot{\theta}_y + \dfrac{\partial \dot{w}_0}{\partial y}\right)^2\right] \end{array} \right\} dx\,dy \tag{12}$$

where the moments of inertia I_n ($n = 0, 1, 2, \ldots, 6$) are defined as:

$$I_n = \sum_{k=1}^{N_L} \int_{z_k}^{z_{k+1}} \rho^{(k)}(z)\, z^n\, dz; \quad n = 0, 1, 2, 3, 4, 6$$

The work done by an external transverse load $q_0(x, y, t)$ is:

$$W = \int_0^a \int_0^b q_0(x, y, t)\, w_0(x, y, t)\, dx\, dy \tag{13}$$

2.5. Pb-2 Ritz solution and governing equations

By applying the pb-2 Ritz method [25], the mid-plane displacement components are approximated by finite series of admissible trial functions expressed in terms of normalized coordinates $\left(\xi = \dfrac{2x}{a} - 1, \eta = \dfrac{2y}{b} - 1\right)$:

$$\begin{aligned} u_0 &= \sum_{p=0}^{N}\sum_{q=0}^{p} d_{1pq} u_{0pq}(\xi, \eta) = \sum_{i=1}^{M} d_{1i} u_{0i}(\xi, \eta) = \mathbf{d}_1^T \mathbf{U} \\ v_0 &= \sum_{p=0}^{N}\sum_{q=0}^{p} d_{2pq} v_{0pq}(\xi, \eta) = \sum_{i=1}^{M} d_{2i} v_{0i}(\xi, \eta) = \mathbf{d}_2^T \mathbf{V} \\ w_0 &= \sum_{p=0}^{N}\sum_{q=0}^{p} d_{3pq} w_{0pq}(\xi, \eta) = \sum_{i=1}^{M} d_{3i} w_{0i}(\xi, \eta) = \mathbf{d}_3^T \mathbf{W} \\ \theta_x &= \sum_{p=0}^{N}\sum_{q=0}^{p} d_{4pq} \theta_{xpq}(\xi, \eta) = \sum_{i=1}^{M} d_{4i} \theta_{xi}(\xi, \eta) = \mathbf{d}_4^T \boldsymbol{\varphi} \\ \theta_y &= \sum_{p=0}^{N}\sum_{q=0}^{p} d_{5pq} \theta_{ypq}(\xi, \eta) = \sum_{i=1}^{M} d_{5i} \theta_{yi}(\xi, \eta) = \mathbf{d}_5^T \boldsymbol{\psi} \end{aligned} \tag{14}$$

where N is the polynomial degree; $d_{ji}(t)$ are time-dependent generalized coordinates – j denotes the displacement component, and i is the corresponding basis-function index, and can be obtained as:

$$i = \frac{(p+1)(p+2)}{2} - (p - q) \tag{15}$$

The total number M of polynomial terms corresponding to polynomial degree N is:

$$M = \frac{1}{2}(N+1)(N+2) \tag{16}$$

The basic functions are constructed as products of a boundary-compliant function $B_j(\xi,\eta)$ set as [25]:

$$\begin{cases} u_{0i} = \xi^{p-q}\eta^q B_u(\xi,\eta) \\ v_{0i} = \xi^{p-q}\eta^q B_v(\xi,\eta) \\ w_{0i} = \xi^{p-q}\eta^q B_w(\xi,\eta) \\ \theta_{xi} = \xi^{p-q}\eta^q B_x(\xi,\eta) \\ \theta_{yi} = \xi^{p-q}\eta^q B_y(\xi,\eta) \end{cases} \tag{17}$$

in which $B_u(\xi,\eta), B_v(\xi,\eta), B_w(\xi,\eta), B_x(\xi,\eta), B_y(\xi,\eta)$ represent basic functions that inherently satisfy boundary conditions (BCs) through the product of boundary expressions and are determined by:

$$\begin{cases} B_u(\xi,\eta) = (\eta+1)^{\mu_1}(\xi-1)^{\mu_2}(\eta-1)^{\mu_3}(\xi+1)^{\mu_4} \\ B_v(\xi,\eta) = (\eta+1)^{\mu_5}(\xi-1)^{\mu_6}(\eta-1)^{\mu_7}(\xi+1)^{\mu_8} \\ B_w(\xi,\eta) = (\eta+1)^{\mu_9}(\xi-1)^{\mu_{10}}(\eta-1)^{\mu_{11}}(\xi+1)^{\mu_{12}} \\ B_x(\xi,\eta) = (\eta+1)^{\mu_{13}}(\xi-1)^{\mu_{14}}(\eta-1)^{\mu_{15}}(\xi+1)^{\mu_{16}} \\ B_y(\xi,\eta) = (\eta+1)^{\mu_{17}}(\xi-1)^{\mu_{18}}(\eta-1)^{\mu_{19}}(\xi+1)^{\mu_{20}} \end{cases} \tag{18}$$

where the exponent μ_k $(k = 0, 1, 2)$ at each edge is assigned according to the boundary condition type:

- $\mu = 0$: For free edge (F),
- $\mu = 1$: For simply supported edge (S),
- $\mu = 2$: For clamped edge (C).

Substituting the Ritz approximations Eqs. (14) into energy functional Eq. (10) and applying Lagrange's equations of motion for each generalized coordinate d_{ji}:

$$\frac{\partial \Pi}{\partial d_{ji}} - \frac{d}{dt}\left(\frac{\partial \Pi}{\partial \dot{d}_{ji}}\right) = 0; \qquad j = 1,2,3,4,5; \qquad i = 1,2,3,\ldots,M \tag{19}$$

The governing equations are obtained in matrix form:

$$\mathbf{M}\ddot{\mathbf{d}} + \mathbf{K}\mathbf{d} = \mathbf{F} \tag{20}$$

where $\mathbf{M}$ is the global mass matrix, $\mathbf{K}$ is the global stiffness matrix, $\mathbf{F}$ is the external load vector, and $\mathbf{d}$ is the vector of displacement coefficients.

$$\mathbf{K} = \begin{bmatrix} \mathbf{K}^{uu} & \mathbf{K}^{uv} & \mathbf{K}^{uw} & \mathbf{K}^{ux} & \mathbf{K}^{uy} \\ \mathbf{K}^{vu} & \mathbf{K}^{vv} & \mathbf{K}^{vw} & \mathbf{K}^{vx} & \mathbf{K}^{vy} \\ \mathbf{K}^{wu} & \mathbf{K}^{wv} & \mathbf{K}^{ww} & \mathbf{K}^{wx} & \mathbf{K}^{wy} \\ \mathbf{K}^{xu} & \mathbf{K}^{xv} & \mathbf{K}^{xw} & \mathbf{K}^{xx} & \mathbf{K}^{xy} \\ \mathbf{K}^{yu} & \mathbf{K}^{yv} & \mathbf{K}^{yw} & \mathbf{K}^{yx} & \mathbf{K}^{yy} \end{bmatrix}; \qquad \mathbf{d} = \begin{Bmatrix} \mathbf{d_1} \\ \mathbf{d_2} \\ \mathbf{d_3} \\ \mathbf{d_4} \\ \mathbf{d_5} \end{Bmatrix}$$

$$\mathbf{M} = \begin{bmatrix} \mathbf{M}^{uu} & \mathbf{0} & \mathbf{M}^{uw} & \mathbf{M}^{ux} & \mathbf{0} \\ \mathbf{0} & \mathbf{M}^{vv} & \mathbf{M}^{vw} & \mathbf{0} & \mathbf{M}^{vy} \\ \mathbf{M}^{wu} & \mathbf{M}^{wv} & \mathbf{M}^{ww} & \mathbf{M}^{wx} & \mathbf{M}^{wy} \\ \mathbf{M}^{xu} & \mathbf{0} & \mathbf{M}^{xw} & \mathbf{M}^{xx} & \mathbf{0} \\ \mathbf{0} & \mathbf{M}^{yv} & \mathbf{M}^{yw} & \mathbf{0} & \mathbf{M}^{yy} \end{bmatrix}; \qquad \mathbf{F} = \begin{Bmatrix} \mathbf{0} \\ \mathbf{0} \\ \mathbf{F}^{w} \\ \mathbf{0} \\ \mathbf{0} \end{Bmatrix} \tag{21}$$

For free vibration analysis, $F = 0$ and harmonic motion $\mathbf{d} = \overline{\mathbf{d}}e^{i\omega t}$; substitution into Eq. (20) leads to the generalized eigenvalue problem:

$$\left(\mathbf{K} - \omega^2\mathbf{M}\right)\overline{\mathbf{d}} = \mathbf{0} \tag{22}$$

from which the natural frequencies ω and corresponding mode shapes $\overline{\mathbf{d}}$ are extracted.

For the transient response, Rayleigh damping is adopted, in which the damping matrix $\mathbf{C}$ is expressed as a linear combination of the mass and stiffness matrices: $\mathbf{C} = a_0\mathbf{M} + a_1\mathbf{K}$. Consequently, the governing equation of motion in Eq. (20) is expressed as:

$$\mathbf{M}\ddot{\mathbf{d}} + \mathbf{C}\dot{\mathbf{d}} + \mathbf{K}\mathbf{d} = \mathbf{F} \tag{23}$$

Assuming that the first two vibration modes share the same damping ratio ξ, the coefficients a_0 and a_1 are determined from the first two natural frequencies ω_1 and ω_2 as [26]:

$$\begin{Bmatrix} a_0 \\ a_1 \end{Bmatrix} = \frac{2\xi}{\omega_1 + \omega_2} \begin{Bmatrix} \omega_1\omega_2 \\ 1 \end{Bmatrix}$$

To evaluate the dynamic response, the Newmark direct integration scheme with time step Δt is adopted. The displacement time histories are computed by solving the governing equations under the following initial state: $d_{ji}(0) = 0$ and $\dot{d}_{ji}(0) = 0$. From this solution, the time history of displacement, velocity, acceleration, and internal stress resultants can be determined for any point on the plate.

3. Convergence study and theoretical validation

Consider a rectangular sandwich plate with length a, width b, and total thickness h. The boundary conditions along each edge are denoted by S, C, and F, corresponding to simply supported, clamped, and free edges, respectively.

3.1. Convergence study

This section examines the convergence and accuracy of the proposed semi-analytical model. The sandwich plate considered for the theoretical convergence benchmark consists of an aluminum foam core [4]: ($E_c = 69$ GPa, $\rho_c = 2707$ kg/m^3, $\nu_c = 0.3$) and CFRP face sheets [24]: ($E_{11} = 25E_{22}$, $E_{22} = 12.1$ GPa, $G_{12} = G_{13} = 0.5E_{22}$, $G_{23} = 0.2E_{22}$, $\nu_{12} = 0.25$, $\rho_f = 1588$ kg/m^3) arranged in the cross-ply configuration [90°/0°/Core/0°/90°]. The geometric parameters are selected as $h_f : h_c : h_f = 1 : 8 : 1$, $a/b = 2.5$, and $a/h = 10$, with a uniform porosity coefficient $e_0 = 0.6$, under various boundary conditions. Table 1 demonstrates the convergence of the non-dimensional fundamental frequency with increasing Ritz expansion order N. The results indicate that the proposed solution converges rapidly, and the frequency values become essentially stable at $N = 10$. To ensure sufficient numerical accuracy, $N = 12$ is adopted for all subsequent calculations.

Table 1. Convergence of the non-dimensional fundamental frequency $\bar{\omega} = \omega\dfrac{a^2}{h}\sqrt{\dfrac{\rho_{\text{core}}}{E_{\text{core}}}}$ with increasing Ritz expansion order N

N	SSSS	CCCC	SFSF	SCSC
1	18.8866	42.9335	5.7832	18.8866
2	18.7632	42.3874	5.6670	18.7632

N	SSSS	CCCC	SFSF	SCSC
3	18.7632	41.6531	5.2452	18.7632
4	18.7630	41.4773	5.2446	18.7630
5	18.7630	41.2046	5.2436	18.7630
6	18.7630	41.1577	5.2435	18.7630
7	18.7630	41.0476	5.2435	18.7630
8	18.7630	41.0331	5.2435	18.7630
9	18.7630	40.9950	5.2435	18.7630
10	18.7630	40.9906	5.2434	18.7630
11	18.7630	40.9796	5.2434	18.7630
12	18.7630	40.9784	5.2434	18.7630

3.2. Free vibration validation

A SSSS square FGP plate with an asymmetric porosity distribution (Type 3) is first validated against the results reported by Thang et al. [7]. The material properties are as follows: $E_1 = 200$ GPa, $\rho_1 = 7850$ kg/m^3, $\nu = 1/3$. The open-cell porosity model is adopted to ensure consistency with the reference study. The non-dimensional frequency is defined as $\bar{\omega} = \omega h \sqrt{\rho_1/E_1}$. Table 2 compares the present results with those obtained by Thang et al. using FSDT and Navier solution for various porosity coefficients and two thickness ratios. Excellent agreement between the two sets of results is observed, thereby confirming the accuracy of the present formulation.

Table 2. Comparison of non-dimensional frequency $\bar{\omega}$ for a SSSS FGP plate

a/h	$e_0 = 0.1$	$e_0 = 0.3$	$e_0 = 0.5$	$e_0 = 0.7$
		$a/h = 5$		
Thang et al. [7]	0.2138	0.2067	0.1978	0.1853
Present	0.2074	0.2004	0.1916	0.1791
		$a/h = 10$		
Thang et al. [7]	0.0574	0.0555	0.0531	0.0495
Present	0.0568	0.0549	0.0525	0.0489

A further benchmark study is performed by comparing the present results with the finite element solutions reported by Thai and Choi [27] for square isotropic alumina plates with material properties $E = 380$ GPa, $\rho = 3800$ kg/m^3, $\nu = 0.3$. The non-dimensional frequency is defined as $\bar{\omega} = \left(\omega a^2 \sqrt{\rho/E}\right)/h$. As shown in Table 3, the present model yields results in close agreement with the reference data for CCCC, SSSS, and SFSF boundary conditions over a range of thickness ratios ($a/h = 5$, 10, and 20).

Finally, an additional validation study is conducted to verify the accuracy and reliability of the proposed RTSDT-pb2 Ritz model through comparison with the well-established FSDT solutions presented by Reddy [24]. The non-dimensional frequency is defined as $\bar{\omega} = \left(\omega b^2 \sqrt{\rho/E}\right)/h$. The benchmark problem considers square laminated composite plates ($a/b = 1$) with material properties ($E_1 = 40E_2$, $G_{12} = G_{13} = 0.6E_2$, $G_{23} = 0.5E_2$, $\nu_{12} = 0.25$) for both antisymmetric cross-ply [0°/90°] and angle-ply [±45°] laminates. As presented in Table 4, the present results exhibit excellent agreement with those reported by Reddy [24], demonstrating the capability and robustness of the proposed formulation in predicting the free vibration characteristics of laminated composite plates under various boundary conditions.

Table 3. Comparison of $\bar{\omega}$ for isotropic plate under various boundary conditions

Boundary condition	Method	$a/h = 5$	$a/h = 10$	$a/h = 20$
CCCC	Thai and Choi [27]	8.0606	9.6604	10.2598
CCCC	Present	8.0946	9.8527	10.5856
SSSS	Thai and Choi [27]	5.2718	5.7576	5.9073
SSSS	Present	5.2611	5.7613	5.9175
SFSF	Thai and Choi [27]	2.7045	2.8331	2.8689
SFSF	Present	2.7118	2.8548	2.8977

Table 4. Comparison of non-dimensional frequency $\bar{\omega}$ for laminated plate under various boundary conditions

$a/h = 10$	SSSS	SCSC	SFSF	SSSF
		Cross-ply [0°/90°]		
Reddy [24]	10.473	15.152	6.881	7.215
Present	10.568	15.712	6.912	7.277
		Angle-ply [±45°]		
Reddy [24]	13.04	15.63	4.76	7.13
Present	13.44	16.33	4.45	6.68

3.3. Transient response validation

The transient response is validated against the results reported by Shen et al. [28]. The benchmark problem considers an isotropic SSSS square plate with material and geometric properties given by $E = 70.3$ GPa, $a = b = 2.438$ m, $h = 6.35$ mm. The plate is subjected to a uniform step load $q = 48.82$ Pa applied over the time interval $0 \leq t \leq 0.2$ s. The time integration is performed using the Newmark scheme with 105 time steps. Fig. 2 compares the time history of the central deflection obtained from the present formulation with the reference solution reported by Shen et al. [28]. The two response curves are found to be in excellent agreement and are nearly indistinguishable throughout the loading duration.

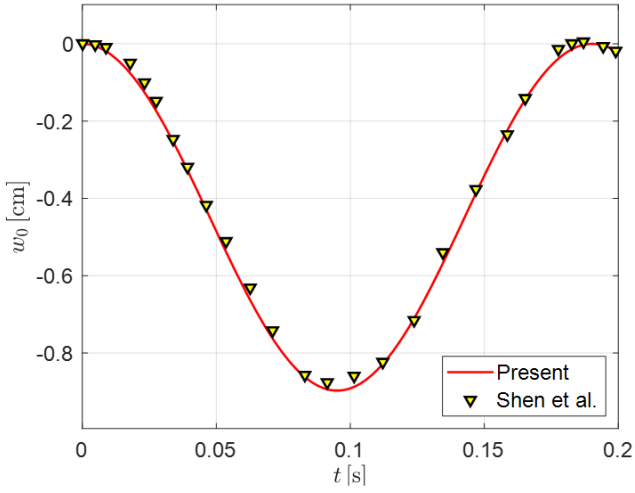


Figure 2. Central deflection history: comparison with Shen et al. [28]

The above validation studies confirm the accuracy and reliability of both the proposed theoretical

formulation and the MATLAB implementation, thereby providing a solid foundation for the subsequent numerical and experimental investigations.

4. Experimental verification of theoretical predictions

4.1. Specimen preparation

The sandwich plate specimens were fabricated using a porous concrete panel supplied by NUCE-WALL as the core material, which was bonded to CFRP face sheets using the hand lay-up technique. The core material consists of lightweight concrete containing EPS beads, resulting in a closed-cellular porous microstructure [23]. The overall specimen dimensions of the specimens are $a \times b \times h = 1000 \times 400 \times 76$ mm, where the core thickness $h_c = 70$ mm and the thickness of each CFRP face sheet is approximately $h_f \approx 3$ mm, comprising multiple laminate plies.

The material properties of the EPS lightweight concrete core were experimentally determined through compression tests conducted on standard cylindrical specimens with dimensions of 15×30 cm. The experimental procedure followed the RILEM CPC 19 recommendations, employing a cyclic loading protocol to evaluate the static modulus of elasticity [29]. This testing approach minimizes the influence of initial microstructural adjustments and nonlinear deformation behavior typically associated with highly porous cementitious composites, thereby providing a more reliable estimate of the effective Young's modulus. The experimental results obtained from the tested specimens are summarized in Table 5. The average Young's modulus was measured as 3.425 GPa, while the recorded peak loads ranged from 7.65 to 8.12 kN. The Poisson ratio of the EPS concrete was assumed to be $\nu = 0.3$.

Table 5. Experimental elastic modulus of the EPS concrete core

Specimen	Dimension (cm)	Peak load (kN)	Elastic modulus E (GPa)
01	15×30	8.12	3.385
02	15×30	7.65	3.442
03	15×30	7.98	3.448
Average		7.92	3.425

The mechanical properties of the cementitious matrix (Grade 100 mortar) were adopted as $E_1 = 14.5$ GPa, and $\rho_1 \approx 1800$ kg/m^3. Based on the theoretical formulation, the porosity coefficient e_0 of the EPS concrete can be determined from the following Eq. (2):

$$e_0 = 1 - \frac{E_2}{E_1} = 1 - \frac{3.425}{14.5} = 0.764 \tag{24}$$

The corresponding mass density coefficient e_m for the closed-cell porous model is calculated using Eq. (4):

$$e_m = 1.121\left(1 - \sqrt[2.3]{1 - e_0}\right) = 0.521 \tag{25}$$

Accordingly, the effective mass density of the EPS concrete can be theoretically evaluated through the mass density coefficient e_m as follows:

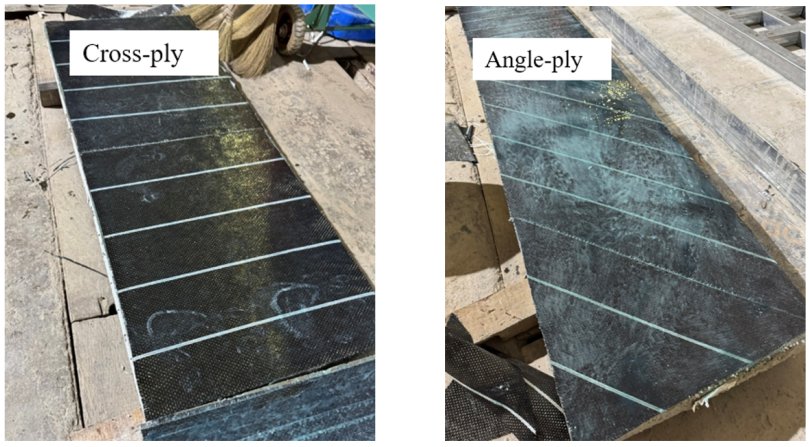
$$e_m = 1 - \frac{\rho_2}{\rho_1} \Rightarrow \rho_2 = \rho_1 (1 - e_m) = 862.02\,\text{kg/m}^3 \tag{26}$$

The CFRP face sheets were fabricated using Toray UT70-30G unidirectional prepreg tape. Because the complete orthotropic properties of the cured UT70-30G laminate were not experimentally characterized in the present study, the effective lamina properties reported by Memarzadeh et al. [30],

for a similar epoxy carbon UD CFRP prepreg system. The corresponding material properties are E_{11} = 121 GPa, E_{22} = 8.6 GPa, $G_{13} = G_{12}$ = 4.7 GPa, G_{23} = 3.1 GPa, ν_{12} = 0.27, ρ = 1588 kg/m^3. Two symmetric laminate configurations are considered in this study, namely the angle-ply configuration $[\pm 45^\circ]_s$ and the cross-ply configuration $[0^\circ/90^\circ]_s$. The CFRP face sheets were bonded to the porous core using an epoxy adhesive, and the assembled specimens were cured under ambient laboratory conditions for 7 days prior to testing. The fabricated sandwich plate specimens are illustrated in Fig. 4.



Figure 3. Experimental setup for uniaxial compression tests and strain measurement of cylindrical EPS concrete specimens according to RILEM CPC 19



(a) Cross-ply specimen (b) Angle-ply EPS sandwich plate

Figure 4. Specimens

It is worth noting that the thin epoxy adhesive layer between the CFRP face sheets and the EPS concrete core is neglected in the displacement field formulation by assuming a perfectly bonded interface. This simplification is adopted to maintain mathematical simplicity and computational efficiency in the global dynamic analysis, since the adhesive layer thickness is very small compared with the overall sandwich plate thickness. Nevertheless, in practical structures, the adhesive layer may exhibit viscoelastic behavior, nonuniform thickness, imperfect bonding, or local interfacial debonding, which can introduce additional compliance and damping effects. These effects may slightly reduce the ef-

fective stiffness of the sandwich plate and partially contribute to the discrepancies observed between the theoretical predictions and experimental results. Therefore, the influence of the adhesive layer is discussed in the interpretation of the experimental frequency discrepancies.

4.2. Test setup and procedure

The vibration test is conducted for a plate supported along the two short edges, corresponding to an SFSF boundary condition. This configuration was selected because it provides a practical and reproducible support condition that closely approximates the analytical SFSF model.

Five KYOWA Electronic Instruments accelerometers were mounted on the top surface of the plate: two at the support locations (channels 1 and 5), two at the quarter-span positions (channels 2 and 4), and one at the plate center (channel 3). The accelerometers are connected to a National Instruments (NI) cDAQ data acquisition system operating at a sampling frequency of 2560 Hz. This sampling rate satisfies the Nyquist criterion, as it exceeds twice the highest frequency of interest [31].

Free vibration was excited using the step-release method. A concentrated mass of 10 kg was suspended at the center of the plate using a thin wire, which was subsequently cut abruptly. The sudden release of the static load generated a transient free vibration response dominated primarily by the fundamental vibration mode.

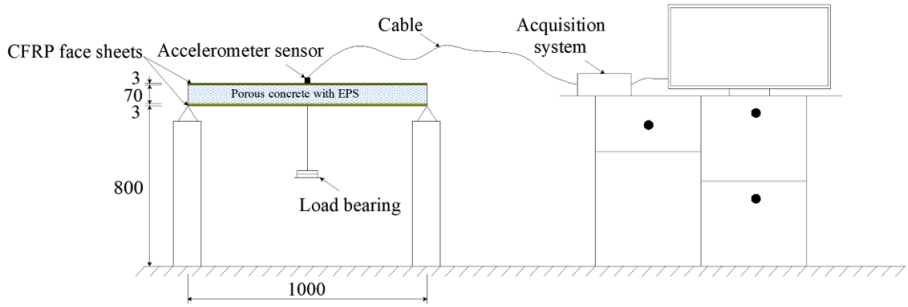


Figure 5. Schematic of the vibration test setup (unit: mm)

The recorded acceleration-time history at the plate center was processed using the Fast Fourier Transform (FFT) technique to identify the fundamental natural frequency. A Hanning window was applied to minimize spectral leakage, while the frequency resolution was determined as approximately $f_s/N = 0.625$ Hz ($N = 4096$) [32]. The experimental setup and the installed sandwich plate specimen are illustrated in Figs. 5 and 6, respectively.

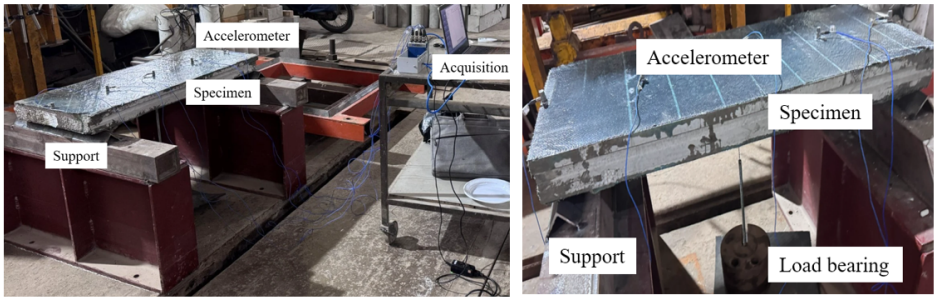


Figure 6. Installed plate and accelerometer layout

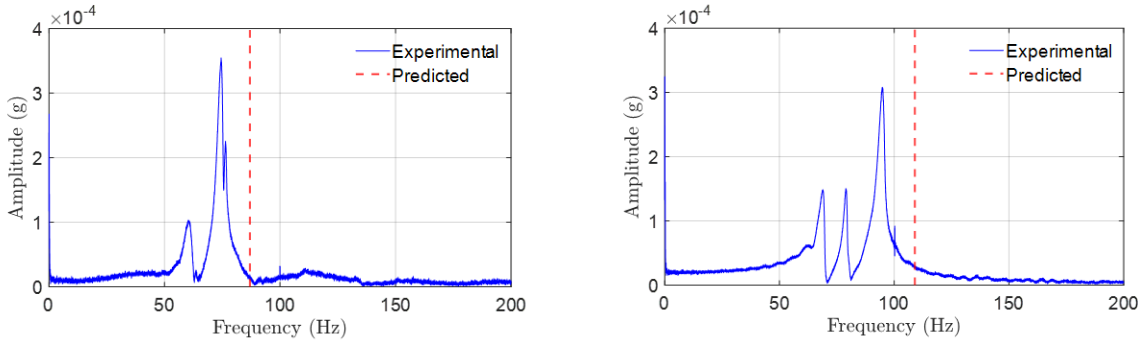
4.3. Experimental results and theoretical prediction

a. Natural frequency

The measured fundamental natural frequencies for the two sandwich plate configurations are summarized in Table 6. The corresponding FFT spectra obtained from representative tests are presented in Fig. 7.

Table 6. Fundamental natural frequency of specimens

Angle-ply specimen			Cross-ply specimen			Theoretical prediction	
1st	2nd	3rd	1st	2nd	3rd	Angle-ply	Cross-ply
75.7	75.3	75.9	91.2	91.3	91.5	87.02	106.86
Average		75.63	Average		91.3		
Discrepancy (%)		13.09	Discrepancy (%)		14.56		



(a) Angle-ply specimen (b) Cross-ply specimen

Figure 7. FFT analysis of the acceleration signal measured at the plate center

As shown in Table 6, the experimental results exhibit good repeatability, with variations of less than 1% among repeated measurements for both laminate configurations. The theoretical predictions are also listed in Table 6 for comparison. The discrepancies between the theoretical and experimental results are approximately 13.09% for the angle-ply sandwich plate and 14.56% for the cross-ply sandwich plate.

The observed discrepancies may be attributed to several idealized modeling assumptions and experimental uncertainties. In the theoretical model, perfect interlayer bonding between the CFRP laminates and the cementitious core is assumed, whereas the actual adhesive layer may exhibit local debonding, nonuniform thickness, and reduced stiffness, leading to a softer structural response. In addition, the mathematically ideal SFSF boundary conditions adopted in the analysis cannot be perfectly reproduced in the experimental setup, which may further reduce the measured frequencies. Moreover, uncertainties in the orthotropic material properties of manually fabricated hand lay-up CFRP laminates, together with fabrication-induced imperfections such as voids in the cementitious matrix, slight geometric deviations, and material inhomogeneity, also contribute to the observed discrepancies between theoretical and experimental results.

b. Acceleration-time history

In addition to the identification of the fundamental frequency, the acceleration-time history at the plate center (channel 3) was recorded to evaluate the transient dynamic response of the sandwich

plates. In the step-release procedure, a static concentrated load P was initially suspended at the plate center using a thin wire. Under this static load, the plate deformed to an equilibrium configuration $\mathbf{d}(0) = \mathbf{d}_{\text{static}}$, which satisfies:

$$\mathbf{K}\,\mathbf{d}_{\text{static}} = \mathbf{F}_{\text{static}} \tag{27}$$

where $\mathbf{F}_{\text{static}}$ denotes the generalized force vector corresponding to the concentrated load P applied at the plate center. When the supporting wire was abruptly cut at $t = 0$, the external load was instantaneously removed, and the plate underwent free vibration from the initially deformed configuration. The corresponding initial conditions ($t = 0$) for the transient analysis are given by:

$$\mathbf{d}(0) = \mathbf{d}_{\text{static}}; \qquad \dot{\mathbf{d}}(0) = \mathbf{0} \tag{28}$$

For $t > 0$, the free vibration response of the damped system is governed by:

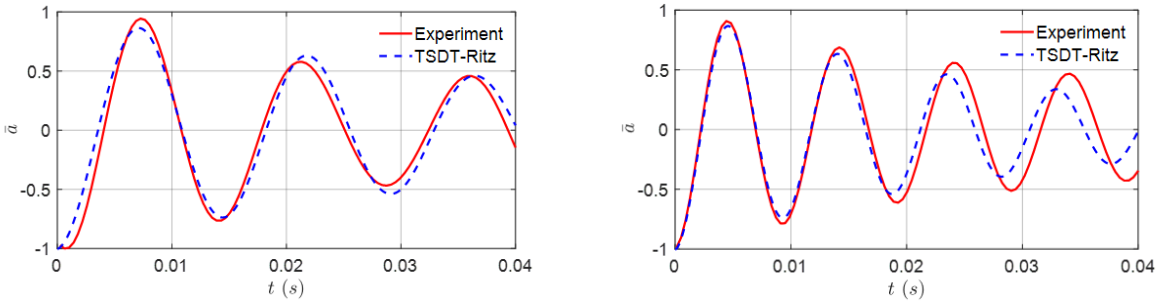
$$\mathbf{M}\,\ddot{\mathbf{d}}(t) + \mathbf{C}\,\dot{\mathbf{d}}(t) + \mathbf{K}\,\mathbf{d}(t) = \mathbf{0} \tag{29}$$

The transient response was numerically integrated using the Newmark constant-average -acceleration scheme with a time increment of $\Delta t = 0.001$ s, which ensures adequate spectral fidelity for frequencies up to 500 Hz. When experimental damping data are available, the damping ratio ξ can be estimated from the decay of the measured free vibration response using the logarithmic decrement method [26]:

$$\xi = \frac{1}{2\pi j} \ln \frac{w_i}{w_{i+j}} \tag{30}$$

where w_i and w_{i+j} denote the displacement amplitudes corresponding to the i-th and $(i+j)$-th vibration cycles, respectively. In the present study, the measured peak amplitudes yielded a damping ratio of approximately $\xi \approx 6.62\%$. This value was subsequently employed to determine the Rayleigh damping coefficients a_0 and a_1 using the first two computed natural frequencies ω_1 and ω_2. To ensure consistency in the transient dynamic simulations, damping ratio $\xi \approx 6.62\%$ was applied to determine the Rayleigh damping coefficients for both the angle-ply and cross-ply configurations. This approach is justified because the structural energy dissipation in this sandwich system is heavily dominated by the viscoelastic nature of the core material (EPS porous concrete) and the epoxy adhesive layer, whereas the fiber orientation angles within the thin CFRP face sheets have a negligible impact on the global damping capacity.

The measured acceleration-time histories at the plate center of both sandwich plate specimens subjected to the step-release test are presented in Fig. 8. To facilitate a clear comparison of the phase and frequency characteristics, the acceleration amplitudes obtained from both the theoretical prediction and experimental measurement were normalized. For both laminate configurations, the theoretical and experimental responses exhibit good agreement during the initial vibration cycle. However, slight differences in the time intervals between successive peaks can be observed, indicating discrepancies in the predicted vibration periods. This deviation becomes more pronounced in the cross-ply specimen. In both cases, the experimental response exhibits a gradual phase delay relative to the TSDT–Ritz prediction as the vibration progresses. Moreover, the cross-ply specimen (Fig. 8(b)) demonstrates a more noticeable shift in the periodic peak positions compared with the angle-ply specimen (Fig. 8(a)). This larger phase deviation is qualitatively consistent with the larger discrepancy in the fundamental natural frequency obtained for the cross-ply configuration (14.56%) relative to the angle-ply configuration (13.09%).



(a) Angle-ply specimen (b) Cross-ply specimen

Figure 8. Acceleration-time history at the plate center

In summary, the dynamic behavior of the porous sandwich plate obtained from the experimental measurements and that predicted by the RTSDT–Ritz analysis is in reasonable agreement. Although the discrepancies remain noticeable, the comparison shows reasonable consistency in the predicted and measured dynamic behavior. These differences may primarily be attributed to (i) measurement uncertainties and imperfect realization of the boundary conditions in the experimental setup, and (ii) the discrepancy between the idealized theoretical model and the actual fabricated sandwich plate specimens. In particular, the adhesive layer between the porous core and the CFRP face sheets was neglected in the theoretical formulation, although it may influence the overall stiffness and damping characteristics of the structure.

5. Conclusions

In this paper, the dynamic behavior of sandwich plates with an EPS porous concrete core and CFRP face sheets was investigated through both semi-analytical modeling and experimental testing. Reddy's third-order shear deformation theory combined with the pb-2 Ritz method was employed to derive the governing equations, while the Newmark integration scheme was utilized to compute the transient acceleration response. The accuracy and reliability of the proposed formulation were first verified through comparisons with published benchmark solutions for free vibration and transient response. Subsequently, experimental vibration tests were conducted on sandwich plate specimens under SFSF boundary conditions to validate the theoretical predictions in terms of the fundamental natural frequency and acceleration-time history. The obtained results lead to the following main conclusions:

- The proposed RTSDT–Ritz formulation exhibits rapid numerical convergence, with the fundamental frequency becoming essentially stable at $N = 10$;

- The theoretical predictions show reasonable agreement with the experimental measurements for both the fundamental natural frequency and transient dynamic response.

- The progressive phase shift observed in the measured acceleration-time history is consistent with discrepancy in the natural frequency between theoretical and experimental results.

Overall, the experimental data and the theoretically supported model presented in this study provide as useful benchmark references for future investigations on the mechanical behavior of porous sandwich plates with composite face sheets.

Acknowledgment

This research is funded by Hanoi University of Civil Engineering under grant number 27-2026/KHXD-TĐ.

Declaration of generative AI and AI-assisted technologies

During the preparation of this manuscript, the authors used ChatGPT to improve the language and readability of the manuscript. The authors reviewed and edited the output and took full responsibility for the accuracy, originality, and integrity of the manuscript.

References

[1] Chen, D., Kitipornchai, S., Yang, J. (2016). Nonlinear free vibration of shear deformable sandwich beam with a functionally graded porous core. *Thin-Walled Structures*, 107:39–48.

[2] Magnucka-Blandzi, E. (2011). Dynamic stability and static stress state of a sandwich beam with a metal foam core using three modified Timoshenko hypotheses. *Mechanics of Advanced Materials and Structures*, 18(2):147–158.

[3] Kitipornchai, S., Chen, D., Yang, J. (2017). Free vibration and elastic buckling of functionally graded porous beams reinforced by graphene platelets. *Materials & Design*, 116:656–665.

[4] Rezaei, A. S., Saidi, A. R. (2016). Application of Carrera unified formulation to study the effect of porosity on natural frequencies of thick porous-cellular plates. *Composites Part B: Engineering*, 91: 361–370.

[5] Wattanasakulpong, N., Eiadtrong, S. (2022). Transient responses of sandwich plates with a functionally graded porous core: Jacobi–Ritz method. *International Journal of Structural Stability and Dynamics*, 23 (04):2350039.

[6] Yüksel, Y. Z., Akbaş, Ş. D. (2021). Vibration analysis of a sandwich plate with laminated face and porous core layers resting on elastic foundation. *Journal of Innovative Science and Engineering*, 6(1):32–45.

[7] Thang, P. T., Nguyen-Thoi, T., Lee, D., Kang, J., Lee, J. (2018). Elastic buckling and free vibration analyses of porous-cellular plates with uniform and non-uniform porosity distributions. *Aerospace Science and Technology*, 79:278–287.

[8] Dat, N. D., Thanh, N. V., MinhAnh, V., Duc, N. D. (2020). Vibration and nonlinear dynamic analysis of sandwich FG-CNTRC plate with porous core. *Mechanics of Advanced Materials and Structures*, 29(10): 1431–1448.

[9] Li, H., Ren, X., Yu, C., Xiong, J., Wang, X., Zhao, J. (2021). Investigation of vibro-acoustic characteristics of FRP plates with porous foam core. *International Journal of Mechanical Sciences*, 209:106697.

[10] Li, D., Kong, D., Chen, T. (2024). Vibration and stability of functionally graded porous (FGP) sandwich plates under moving mass. *Acta Mechanica*, 235(12):7531–7551.

[11] Safaei, B. (2021). Frequency-dependent damped vibrations of multifunctional foam plates sandwiched and integrated by composite faces. *The European Physical Journal Plus*, 136(6):646.

[12] Said, A. I., Mouwainea, E. M. (2021). Experimental study of reinforced concrete slabs strengthened by CFRP subjected to impact loads. *IOP Conference Series: Earth and Environmental Science*, 856(1): 012002.

[13] Bukhari, I., Vollum, R., Ahmad, S., Sagaseta, J. (2010). Shear strengthening of reinforced concrete beams with CFRP. *Magazine of Concrete Research*, 62(1):65–77.

[14] Jasion, P., Magnucka-Blandzi, E., Szyc, W., Magnucki, K. (2012). Global and local buckling of sandwich circular and beam-rectangular plates with metal foam core. *Thin-Walled Structures*, 61:154–161.

[15] Sokolinsky, V. S., Shen, H., Vaikhanski, L., Nutt, S. R. (2003). Experimental and analytical study of nonlinear bending response of sandwich beams. *Composite Structures*, 60(2):219–229.

[16] Sokolinsky, V. S., Von Bremen, H. F., Lavoie, J. A., Nutt, S. R. (2004). Analytical and experimental study of free vibration response of soft-core sandwich beams. *Journal of Sandwich Structures & Materials*, 6 (3):239–261.

[17] Dariushi, S., Sadighi, M. (2014). A new nonlinear high order theory for sandwich beams: An analytical and experimental investigation. *Composite Structures*, 108:779–788.

[18] Njim, E. K., Bakhy, S. H., Al-Waily, M. (2021). Free vibration analysis of imperfect functionally graded sandwich plates: analytical and experimental investigation. *Archives of Materials Science and Engineering*, 111(2):49–65.

[19] Yurddaskal, M., Ozmen, U., Kir, M., Okutan Baba, B. (2018). The effect of foam properties on vibration response of curved sandwich composite panels. *Composite Structures*, 183:278–285.

[20] Zhang, X., Yu, K., Bai, Y., Zhao, R. (2015). Thermal vibration characteristics of fiber-reinforced mullite sandwich structure with ceramic foams core. *Composite Structures*, 131:99–106.
[21] Hung, T. Q., Duc, D. M., Tu, T. M., Dung, L. X., Bao, C. N. (2024). Static and dynamic behaviour of sandwich beams with porous core: Experiment and moving least squares mesh-free analysis. *Journal of Science and Technology in Civil Engineering (JSTCE) - HUCE*, 18(1):39–54.
[22] Gibson, L. J. (2003). Cellular solids. *MRS Bulletin*, 28(4):270–274.
[23] Prasittisopin, L., Termkhajornkit, P., Kim, Y. H. (2022). Review of concrete with expanded polystyrene (EPS): Performance and environmental aspects. *Journal of Cleaner Production*, 366:132919.
[24] Reddy, J. N. (2003). *Mechanics of laminated composite plates and shells: Theory and analysis*. CRC Press.
[25] Wu, L. H., Lu, Y. (2011). Free vibration analysis of rectangular plates with internal columns and uniform elastic edge supports by pb-2 Ritz method. *International Journal of Mechanical Sciences*, 53(7):494–504.
[26] Chopra, A. K. (2017). *Dynamics of structures: Theory and applications to earthquake engineering*. 5th edition edition, Pearson.
[27] Thai, H.-T., Choi, D.-H. (2013). Finite element formulation of various four unknown shear deformation theories for functionally graded plates. *Finite Elements in Analysis and Design*, 75:50–61.
[28] Shen, Z., Xia, J., Cheng, P. (2019). Geometrically nonlinear dynamic analysis of FG-CNTRC plates subjected to blast loads using the weak form quadrature element method. *Composite Structures*, 209: 775–788.
[29] Rilem, T. C. (1994). *RILEM recommendations for the testing and use of constructions materials*. RC, 6, pp. 218–220.
[30] Memarzadeh, A., Onyibo, E. C., Asmael, M., Safaei, B. (2024). Dynamic effect of ply angle and fiber orientation on composite plates. *Spectrum of Mechanical Engineering and Operational Research*, 1(1): 90–110.
[31] Shannon, C. E. (1949). Communication in the presence of noise. *Proceedings of the IRE*, 37(1):10–21.
[32] Meng, B., Shan, G., Zheng, Y. (2023). Design of spectrum processing chiplet based on FFT algorithm. *Micromachines*, 14(2):402.